

Cite as: Appl. Phys. Lett. **118**, 051902 (2021); https://doi.org/10.1063/5.0035298 Submitted: 27 October 2020 . Accepted: 26 December 2020 . Published Online: 02 February 2021

🗓 Jinwook Kim, Sandeep Kasoji, 🗓 Phillip G. Durham, and 🗓 Paul A. Dayton

COLLECTIONS

- F This paper was selected as Featured
- SCI This paper was selected as Scilight







ARTICLES YOU MAY BE INTERESTED IN

Acoustic holograms selectively direct cavitation energy Scilight 2021, 081103 (2021); https://doi.org/10.1063/10.0003579

Lamb wave coupled resonance for SAW acoustofluidics
Applied Physics Letters 118, 051103 (2021); https://doi.org/10.1063/5.0035906

A Perspective on acoustical tweezers—devices, forces, and biomedical applications Applied Physics Letters 117, 180501 (2020); https://doi.org/10.1063/5.0028443





Acoustic holograms for directing arbitrary cavitation patterns () (0)

Cite as: Appl. Phys. Lett. 118, 051902 (2021); doi: 10.1063/5.0035298 Submitted: 27 October 2020 · Accepted: 26 December 2020 · Published Online: 2 February 2021

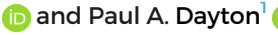








Jinwook Kim,^{1,a)} 🕞 Sandeep Kasoji,² Phillip G. Durham, ¹ 🕞 and Paul A. Dayton ¹ 🕞





AFFILIATIONS

 1 Joint Department of Biomedical Engineering, The University of North Carolina at Chapel Hill and North Carolina State University, Chapel Hill, North Carolina 27599, USA

ABSTRACT

Cavitation is an important phenomenon in biomedical acoustics. It can produce both desired outcomes (i.e., local therapeutic effects in vivo) and undesired outcomes (i.e., tissue damage), and it is, thus, important to both understand and direct cavitation fields. Through the use of three-dimensional-printed acoustic lenses and cavitation-sensitive acoustic phantoms, we demonstrate the generation of arbitrary shape twodimensional (2D) microbubble cavitation fields. In this study, we demonstrate shaping a 1 MHz acoustic beam as the character "7" on a target plane that contains a higher mechanical index than the cavitation threshold for encapsulated microbubbles in a gelatin phantom. The lens pattern is first designed by calculating the phase map of the desired field using an angular spectrum approach. After lens implementation, acoustic pulsing through the lens generated the target acoustic field in a phantom and produced a cavitation map following the intended 2D pattern. The cavitation pattern was similar (with the structural similarity of 0.476) to the acoustic pressure map of the excitation beam.

Published under license by AIP Publishing. https://doi.org/10.1063/5.0035298

Acoustic cavitation is the formation, oscillation, and collapse of bubbles induced by intense ultrasound waves in a liquid medium.¹ Cavitating microbubbles generate local shear forces near bubbles through the mechanisms of microstreaming, microjets, and shock waves.2 The shear forces in a cavitation field have been a versatile tool to promote physical effects in diverse industrial applications, such as surface cleaning,³ particle fragmentation,⁴ emulsification,⁵ and cell disruption. In medical acoustics, cavitation can induce therapeutic effects, such as thermal enhancement or blood-brain barrier opening, or undesired effects, such as vascular hemorrhage or cell destruction. To enhance cavitational effects, perfluorocarbon microbubble contrast agents have been used as cavitation nuclei.8 Since cavitation nuclei significantly reduce the cavitation threshold pressure (peak negative pressure, PNP < 2 MPa) compared to the bubble nucleation threshold, enhanced cavitation effects can be achieved with reduced excitation pressure.5

As the cavitation threshold pressure significantly decreases when using microbubbles, cautious spatial control of the excitation pressure field is required for the separation of the inertial cavitation zone (bubble rupture) from the noncavitation zone. 10 Imprecisely controlled cavitation in vivo could result in severe bioeffects under certain conditions. 11 Precisely shaped acoustic wavefronts with a uniform cavitation threshold could be highly beneficial for spatiotemporally controlled, sonication-based bio-sample processing and cellular level sonoporation studies, as several recent studies emphasize the importance of both spatial specificity and high throughput of cavitation-based biosample processing. 12-16 For example, cavitation-enhanced sonication is employed in preparing samples in a multiwell plate (e.g., 96 or 384 wells), such as genomic-DNA shearing.¹⁵ For high throughput and reliable sample processing, it is crucial to generate a precisely shaped pressure field that induces uniform cavitation dose in each well. In traditional ultrasound techniques, wavefront shaping is realized by controlling the phase and amplitude of multiple elements in an array transducer. The higher spatial resolution of a targeted beam shape requires more array elements, but the number of elements has been limited due to the complexity of transducer circuitry. 19

Recently, using acoustic holograms, acoustic metamaterial lenses manufactured using an inexpensive process have provided an improved spatial resolution of a targeted beam shape.²² An acoustic hologram surface encodes the predefined phase profile as the pixelized thickness profile through high-resolution ($<20 \,\mu m$) threedimensional (3D) printing.^{22,23} This holographic surface is simply assembled with a single-element transducer, and the planar wavefronts diffract through the hologram lens to reconstruct a designed 3D sound

²Triangle Biotechnology, Chapel Hill, North Carolina 27517, USA

a) Author to whom correspondence should be addressed: jinwookk@email.unc.edu

field with diffraction-limited resolution. ^{22,224} With the merits of simple assembly and high resolution compared to conventional array transducers, acoustic holograms have demonstrated the desired spatial controllability in several applications, such as particle manipulation, ^{22,25,26} contactless power transfer, ²⁷ and transcranial ultrasound therapy. ^{28,29} Considering the demonstrated spatial resolution of tailored wavefronts by acoustic holograms, we hypothesized that a hologram lens provides an arbitrary pressure field with the inertial cavitation threshold of microbubbles, and consequently, the desired shape of the cavitation field can be achieved. In this study, we tested this hypothesis by monitoring two-dimensional (2D) microbubble destruction patterns in a gelatin phantom block that contains distributed microbubbles.

We selected the excitation frequency and a source diameter to be 1 MHz and 25.4 mm, respectively, considering the specification of a piston source transducer (IL0108HP, CTS, Hopkinton, MA, USA). Based on the selected frequency and source diameter, we designed acoustic holograms following the previously described simulation procedure using an iterative angular spectrum approach (IASA). ²² Briefly, we set the character 7 as the target shape of the 2D cavitation zone at the distance of 7.5 mm (5 λ , where λ is the wavelength in water), and the phase map at the hologram plane was repeatedly calculated (70 iterations) using the angular spectrum approach until we obtained the desired pressure field at the target plane (see the supplementary

material for further details). The computed phase map and the simulated pressure field are shown in Figs. 1(a) and 1(b), respectively. The phase map was converted to the thickness map considering the wave speed of the hologram material (2424 m/s, standard photopolymer resin, FLGPCL02, Formlabs, Somerville, MA, USA)²⁷ and the acoustic medium (water: 1500 m/s). The thickness map was printed using a 3D printer (Form 2, Formlabs, Somerville, MA, USA), and the printed hologram lens [Fig. 1(c)] was assembled to the piston transducer. We adopted the lens material properties (wave speed: 2424 m/s; density: 1100 kg/m³) from the previous work that used the same 3D-printer and clear resin.²⁷ More detailed information regarding the 3D-printed hologram lens is presented in the supplementary material. We measured the pressure field at the target plane using a hydrophone (HNA-0400, Onda, Sunnyvale, CA, USA) as shown in Fig. 1(d). The pulse condition was a 10-cycle burst at 1 MHz with a 1-s pulse duration (see the supplementary material for beam-mapping details). We used a relatively small source diameter in wavelength of water (16.9 λ) compared to previous works, e.g., 66.7λ (2 MHz and 50 mm)²² and 55.8λ (2.7 MHz and 31 mm).²⁴ Although this small diameter possibly caused relatively low field reconstruction fidelity compared to previous works, multiple focal areas presented a discernable pattern as the targeted seven-shape pattern. We confirmed that the 10-cycle burst pulsing scheme produced almost the same pressure map that is

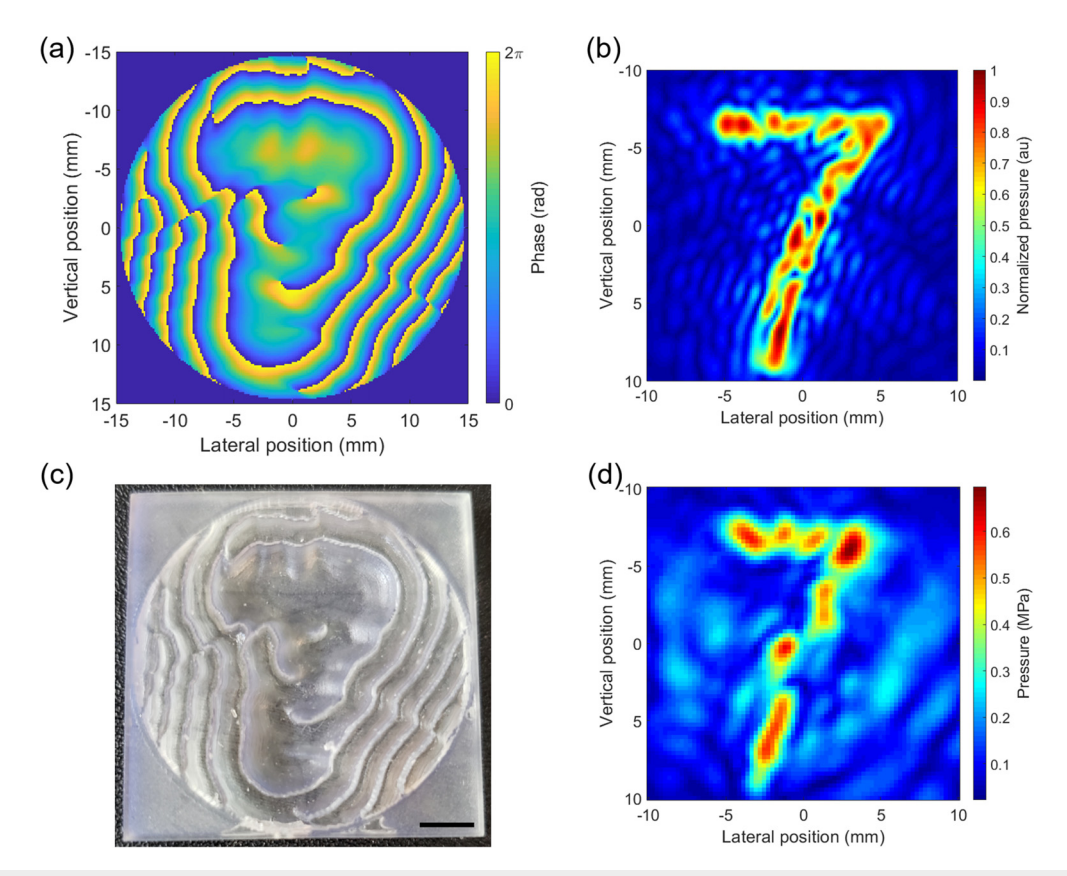


FIG. 1. Simulated and experimental measurement of the patterned pressure field as the character 7: (a) simulated phase profile at the hologram plane, (b) simulated pressure field from the hologram in (a), and (c) a 3D printed hologram lens that encodes the phase information as the thickness profile. The phase 2π in (a) corresponds to the minimum thickness (scale bar: 5 mm). (d) Experimentally measured pressure field transmitted from the hologram lens in (c).

generated by 1000-cycle burst (supplementary material Fig. S3), showing a slight difference in maximum pressure: 678 kPa by 10-cycle burst vs 720 kPa by the 1000-cycle burst. This result indicates that the 10-cycle burst wave is a valid input condition in this study although the angular spectrum method is based on continuous waves. The deviation between the simulated and experimentally measured fields is possibly caused by the nonuniform pressure field of a piston source, effects of the frequency bandwidth in the experiment, 30 different mapping resolutions (133 × 133 in simulation vs 76 × 76 in the experiment), and 3D-printing errors in the thickness map.

To estimate the inertial cavitation zone within the seven-shaped pressure field, we examined the measured field in terms of the mechanical index (MI), which is defined as PNP (MPa) divided by the square root of the excitation frequency (MHz). As the MI involves a trade-off between PNP and excitation frequency of a short pulse (duty cycle < 1%), 1 the MI can be a more comprehensive and reliable measure than PNP alone. In this study, we used in-house lipid-shelled decafluorobutane (DFB) microbubbles with a mean diameter of $1.1 \, \mu \text{m}$. The previously reported rupture threshold of these microbubbles is in the range of $0.25-0.4 \, (\text{MI} > 0.4 \, \text{for assured rupture})$. Hence, we examined the saturated pixels with the saturation thresholds of $0.2, 0.3, 0.4, \text{ and } 0.5, \text{ and each threshold MI was plotted by a$

contour line (Fig. 2). With the threshold MI of 0.3 and 0.4, the cavitation zone also showed the shape of 7. The thresholding results for more substeps of MI thresholds are shown in the supplementary material (Fig. S4). These results indicate that the designed acoustic hologram produced a targeted inertial cavitation zone for microbubbles. Thus, we anticipated that the designed beam destroys the microbubbles mainly within the contours as shown in Figs. 2(b) or 2(c) if microbubbles are distributed in a target plane.

We tested the designed cavitation pattern using a microbubble-gelatin phantom. The phantom was prepared following a similar procedure for a typical tissue-mimicking phantom with the addition of microbubbles. Briefly, we mixed 10 g of bovine skin gelatin powder (G 9382, 225 g Bloom, Sigma Aldrich), 5 g of inulin-based soluble fiber powder (Vitamin Shoppe, Inc., Secaucus, NJ, USA), and 100 ml of distilled water at 45 °C until the powders were completely dissolved. 50 μ l of DFB microbubbles were added to the cooled (<35 °C) gelatin-fiber-solution, and the solution was poured into a custom mold and refrigerated for 12 h. The detailed preparation procedure is described in the supplementary material. According to the raw concentration of in-house microbubbles (approximately 1 × 10¹⁰ bubbles/ml), the estimated microbubble concentration in the phantom is approximately 5×10^6 bubbles/ml. The prepared microbubble phantom was excited

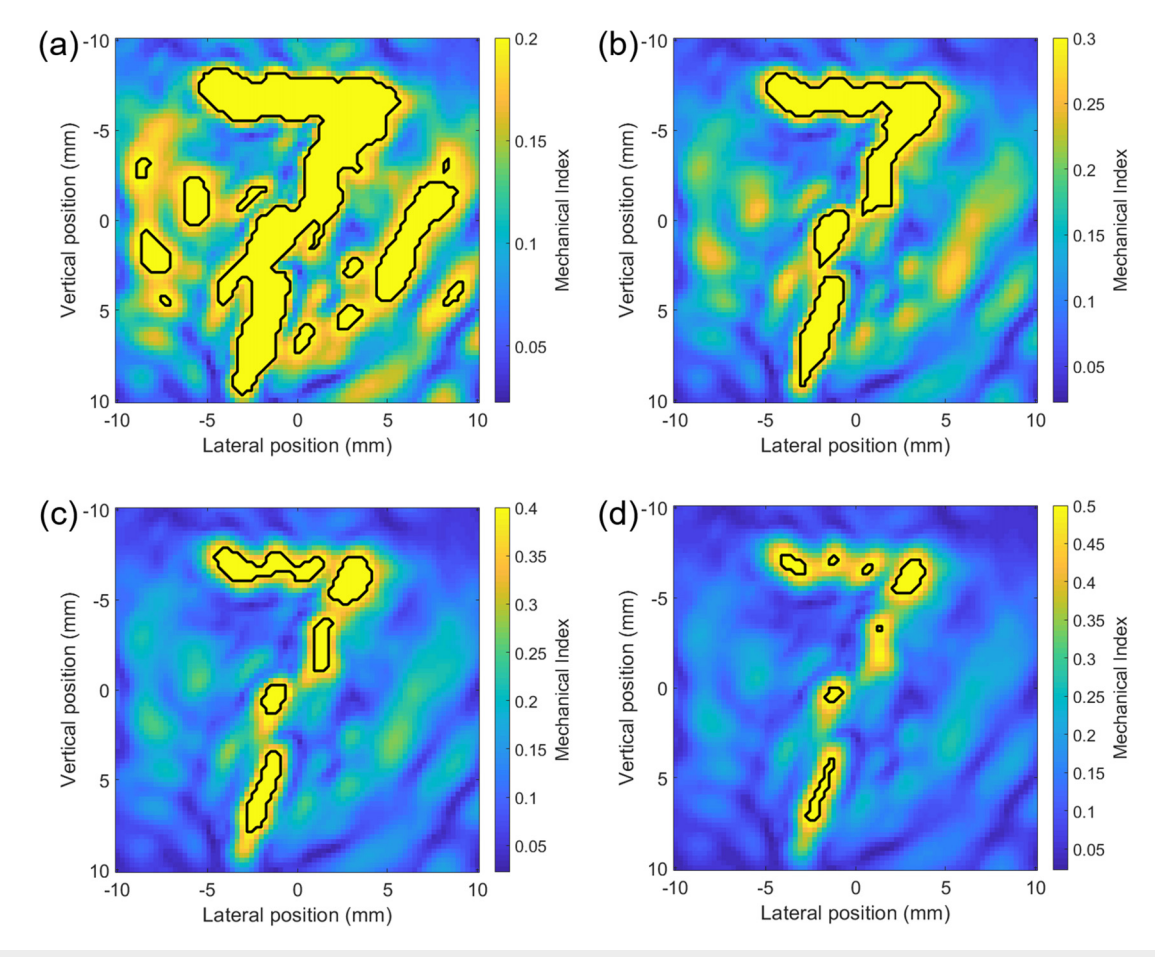


FIG. 2. Estimated inertial cavitation area (black line contours) determined by varying mechanical indices: (a) 0.2, (b) 0.3, (c) 0.4, and (d) 0.5.

using the hologram-conjugated 1 MHz source as shown in the experimental setup (Fig. 3). The test setup also includes a B-mode imaging system (15L8 linear array transducer and Siemens Sequoia 512, Mountain View, CA, USA) to monitor the inertial cavitation pattern at the target plane (5 λ away from the hologram plane). The excitation PNP and pulsing condition were the same (1 MHz, 10 cycles, and 1-s pulse duration) as the condition used for the beam shape measurement [Fig. 1(d)]. The imaging frequency was 14 MHz, and the imaging depth was 40 mm with a 68 dB-dynamic range. We controlled the MI of the imaging pulses as to not induce undesired cavitation by imaging. We observed that an imaging MI around 0.25 exhibited acceptable Bmode images without the destruction of the distributed microbubbles, whereas an imaging MI > 0.4 induced noticeable destruction of microbubbles within the imaging beam size, i.e., 25 mm (lateral) × 40 mm (axial). A primary mechanism of the cavitation pattern is the rupture of distributed microbubbles rather than acoustic radiation forceinduced acoustic streaming, which is caused by applied transient peaknegative (rarefaction) pressure that increases the bubble radius and surface tension.³⁴ Once the surface tension reaches a critical breakup tension by the threshold pressure, the shell ruptures and the microbubble disappears, which is imaged with low brightness in B-mode images.

We acquired 18 images during the excitation of 160 s (averaged time setup of 9 s) and analyzed the bubble destruction zone (regions with reduced microbubble backscatters) in the acquired images. For image processing, we loaded the images in 256 gray levels (48 dB). The representative images before and after the patterned excitation are shown in Fig. 4. The whole acquired images are presented in the supplementary material. Before excitation, the distributed microbubbles were imaged as bright scatterers (averaged grayscale 87.4) at the target plane. After the 34th tone-burst excitation, the scatterers in the seven-shaped pattern started to disappear, which indicated that sufficient PNP for rupturing microbubbles was delivered to the target plane. We

observed a noticeable pattern of the cavitation zone after the 157th excitation. More explicit patterns of inertial cavitation were observed by image thresholding (the grayscale value 45 as a threshold), as shown in the binary images in Fig. 4. For quantitative comparison, we calculated the structural similarity (SSIM) index between the patterned MI maps in Fig. 2 and the acquired cavitation pattern (after the 157th excitation).³⁵ The comparison results showed that the cavitation zone formed a similar shape to the MI map with the threshold of 0.3 (the SSIM index of 0.476). This SSIM index is 1.2-fold of the index for the MI map with the threshold of 0.2 (0.395), which implies that the shaped patterns with an MI lower than 0.2 are not sufficient to generate the designed inertial cavitation pattern. The SSIM indices for 0.4 and 0.5 MI threshold maps were 0.469 and 0.458, respectively. These values are slightly lower but comparable to the case of the 0.3-threshold MI map. We interpreted these results that an MI field higher than 0.3 forms the effective field of inertial cavitation, and this effective field with MI thresholding can be designed by acoustic holograms. The importance of an MI higher than 0.3 is also supported by the previously demonstrated rupture condition of the same composition (lipidshelled DFB core) microbubbles.

We obtained the overall seven-shaped inertial cavitation pattern (with the structural similarity of 0.476) by the tailored acoustic excitation through the acoustic hologram. The deviation between the designed pressure pattern and the cavitation pattern is possibly caused by scattering from the distributed microbubbles in a propagation path (approximately 3 mm in a microbubble-gelatin phantom). Since microbubbles are distributed scatterers, most of the initial pulses were scattered and the waves that arrived at the target plane were likely distorted compared to the designed wavefronts. This consideration corresponds to the results that the initial 10 bursts exhibited only an unnoticeable pattern of bubble ruptures despite the anticipated MI field of up to 0.6. More than 30 bursts can cause the rupture of distributed microbubbles along the propagation path, and thus, the reduced scattering and shading

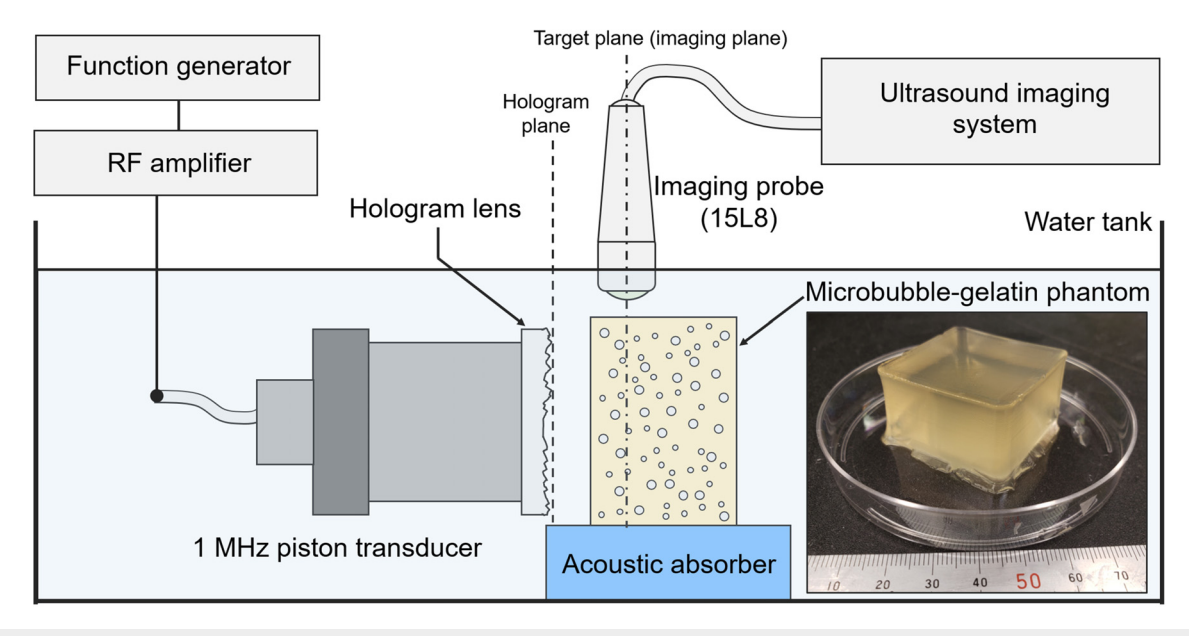


FIG. 3. Experimental setup for multifocal cavitation of microbubbles using the hologram.

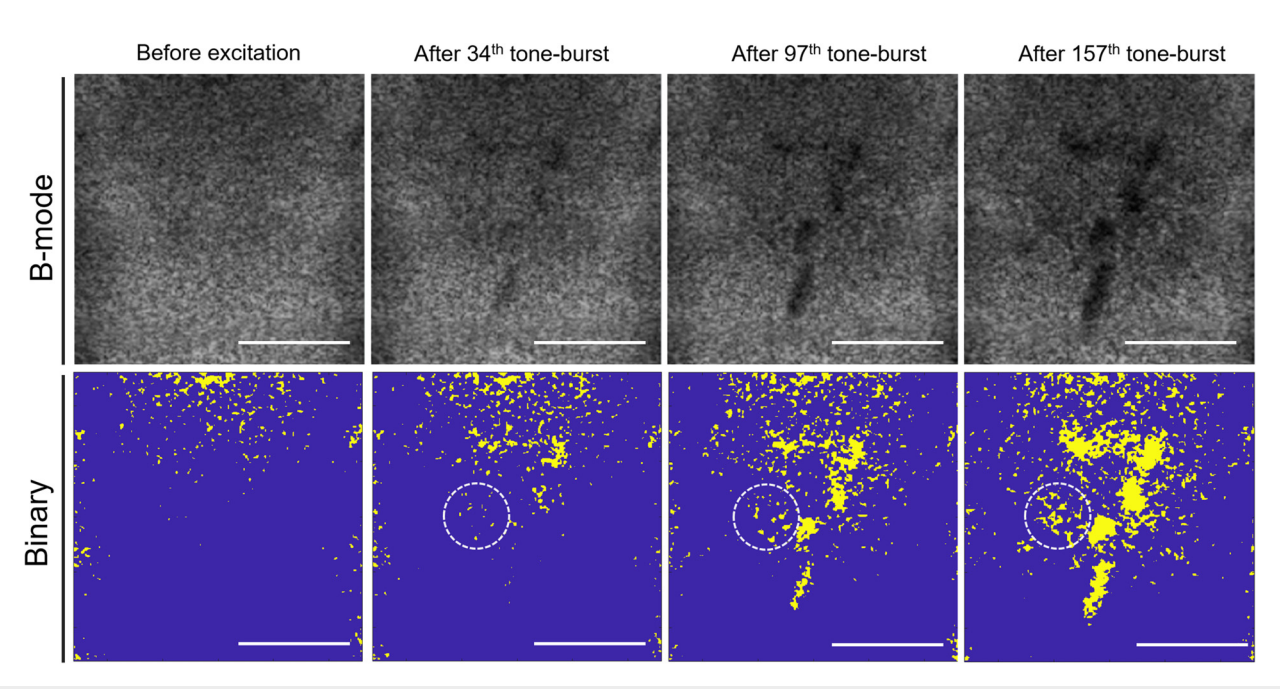


FIG. 4. B-mode images of a microbubble-gelatin phantom before and after multiple tone-burst excitations through the acoustic hologram. The binary images show the patterns of pixels with brightness lower than -26 dB. The dotted circles indicate an example of undesired cavitation (scale bar: 10 mm).

effects can facilitate producing the originally designed cavitation pattern. During the 157 pulses, there was also unintended cavitation in the target plane as marked by dotted circles in Fig. 4. These sporadic cavitations were likely caused by scattered beams and the superposition of synchronized pressure waves in a 1 MHz excitation beam and a 14 MHz imaging beam, which can induce transient PNP higher than the threshold MI. We expect that the enhanced resolution of the shaped wavefronts can reduce the observed errors. The higher resolution of the wavefronts can be achieved by increasing frequency, enlarging the source beam diameter, or utilizing double hologram lenses for both phase and amplitude modulation.²⁴

This work demonstrated that an acoustic hologram can be designed to produce a desired inertial cavitation field shape in a microbubble-distributed gelatin phantom. The identified mechanical index threshold to detect a noticeable shape of microbubble cavitation was 0.3, which corresponds to the previously determined threshold. Although we demonstrated a relatively simple pressure pattern compared to previous studies due to the limited source diameter, our experimental demonstration of patterned cavitation exhibited advantages of acoustic hologram lens over conventional arrays or motorized scanning systems. Simultaneous multifocal patterned cavitation is a crucial advantage for sonication-based bio-sample processing and cellular level sonoporation studies since it enables high spatiotemporal controllability and high throughput. This study focused on a controlled cavitation field in a 2D plane since most site-specific sonoporation studies and multifocal sonication studies focus on a lateral spatial resolution with a small axial dimension of interest. For general cavitation-enhanced therapies, a precisely shaped 3D cavitation field is also important. Thus, this work could be extended to realize arbitrarily shaped 3D cavitation patterns with multifocal planes³⁶ for spatially controllable cavitation-enhanced ultrasound therapies.

See the supplementary material for the illustration of the iterative angular spectrum approach procedure, pressure field measurement procedure, binary maps by thresholding with various mechanical indices, phantom preparation procedure, and acquired B-mode images before image processing.

This work was supported by Grant No. 1938293 from the National Science Foundation.

P.A.D., S.K., and J.K. are inventors on a pending patent describing multifocal sonication using an acoustic hologram lens. P.A.D. and S.K. own equity in Triangle Biotechnology, Inc.

DATA AVAILABILITY

The data that support the findings of this study are available from the corresponding author upon reasonable request.

REFERENCES

- ¹K. Yasui, *Theoretical and Experimental Sonochemistry Involving Inorganic Systems*, edited by M. Ashokkumar (Springer Netherlands, Dordrecht, 2011), pp. 1–29.
- ²S. Mitragotri, Nat. Rev. Drug Discov. 4, 255 (2005).
- ³D. Fernandez Rivas, J. Betjes, B. Verhaagen, W. Bouwhuis, T. C. Bor, D. Lohse, and H. J. G. E. Gardeniers, J. Appl. Phys. 113, 64902 (2013).
- 4S. Guo, X. Du, X. Wang, S. Lu, A. Shi, S. Xu, A. Bouakaz, and M. Wan, Appl. Phys. Lett. 111, 123701 (2017).
- ⁵T. D. Khokhlova, M. S. Canney, V. A. Khokhlova, O. A. Sapozhnikov, L. A. Crum, and M. R. Bailey, J. Acoust. Soc. Am. 130, 3498 (2011).
- ⁶D. R. Mittelstein, J. Ye, E. F. Schibber, A. Roychoudhury, L. T. Martinez, M. H. Fekrazad, M. Ortiz, P. P. Lee, M. G. Shapiro, and M. Gharib, Appl. Phys. Lett. 116, 013701 (2020).
- ⁷ Therapeutic Ultrasound, edited by J.-M. Escoffre and A. Bouakaz (Springer International Publishing, Cham, Switzerland, 2016).
- ⁸B. C. Tran, J. Seo, T. L. Hall, J. B. Fowlkes, and C. A. Cain, IEEE Trans. Ultrason. Ferroelectr. Freq. Control **50**, 1296 (2003).

- ⁹J. Kim, R. M. DeRuiter, L. Goel, Z. Xu, X. Jiang, and P. A. Dayton, Ultrasound Med. Biol. 46, 3059 (2020).
- ¹⁰ J. Kim, B. D. Lindsey, W.-Y. Chang, X. Dai, J. M. Stavas, P. A. Dayton, and X. Jiang, Sci. Rep. 7, 3454 (2017).
- ¹¹D. L. Miller, X. Lu, M. Fabiilli, K. Fields, and C. Dou, Ultrasound Med. Biol. **42**, 1929 (2016).
- ¹²C. W. Barney, C. E. Dougan, K. R. McLeod, A. Kazemi-Moridani, Y. Zheng, Z. Ye, S. Tiwari, I. Sacligil, R. A. Riggleman, S. Cai, J.-H. Lee, S. R. Peyton, G. N. Tew, and A. J. Crosby, Proc. Natl. Acad. Sci. 117, 9157–9165 (2020).
- ¹³F. Li, C. Yang, F. Yuan, D. Liao, T. Li, F. Guilak, and P. Zhong, Proc. Natl. Acad. Sci. 115, E353–E362 (2018).
- ¹⁴M. Thein, A. Cheng, P. Khanna, C. Zhang, E.-J. Park, D. Ahmed, C. J. Goodrich, F. Asphahani, F. Wu, N. B. Smith, C. Dong, X. Jiang, M. Zhang, and J. Xu, Biosens. Bioelectron. 27, 25 (2011).
- ¹⁵S. K. Kasoji, S. G. Pattenden, E. P. Malc, C. N. Jayakody, J. K. Tsuruta, P. A. Mieczkowski, W. P. Janzen, and P. A. Dayton, PLoS One 10, e0133014 (2015).
- ¹⁶S. Yoon, M. G. Kim, C. T. Chiu, J. Y. Hwang, H. H. Kim, Y. Wang, and K. K. Shung, Sci. Rep. 6, 20477 (2016).
- ¹⁷V. Chaplin, M. A. Phipps, and C. F. Caskey, Phys. Med. Biol. **63**, 105016 (2018).
- ¹⁸A. Payne, U. Vyas, N. Todd, J. de Bever, D. A. Christensen, and D. L. Parker, Med. Phys. **38**, 4971 (2011).
- ¹⁹R. E. Davidsen and S. W. Smith, IEEE Trans. Ultrason. Ferroelectr. Freq. Control 45, 338 (1998).
- 20 M. D. Brown, B. T. Cox, and B. E. Treeby, Appl. Phys. Lett. 111, 244101 (2017).

- ²¹P. Kruizinga, P. van der Meulen, A. Fedjajevs, F. Mastik, G. Springeling, N. de Jong, J. G. Bosch, and G. Leus, Sci. Adv. 3, e1701423 (2017).
- ²²K. Melde, A. G. Mark, T. Qiu, and P. Fischer, Nature **537**, 518 (2016).
- ²³M. D. Brown, D. I. Nikitichev, B. E. Treeby, and B. T. Cox, Appl. Phys. Lett. 110, 094102 (2017).
- ²⁴M. D. Brown, Appl. Phys. Lett. **115**, 053701 (2019).
- 25Y. Gu, C. Chen, J. Rufo, C. Shen, Z. Wang, P.-H. Huang, H. Fu, P. Zhang, S. A. Cummer, Z. Tian, and T. J. Huang, ACS Nano 14, 14635 (2020).
- ²⁶Z. Ma, A. W. Holle, K. Melde, T. Qiu, K. Poeppel, V. M. Kadiri, and P. Fischer, Adv. Mater. 32, 1904181 (2020).
- ²⁷M. Bakhtiari-Nejad, A. Elnahhas, M. R. Hajj, and S. Shahab, J. Appl. Phys. 124, 244901 (2018).
- ²⁸G. Maimbourg, A. Houdouin, T. Deffieux, M. Tanter, and J. F. Aubry, Phys. Med. Biol. 63, 135012 (2018).
- ²⁹S. Jiménez-Gambín, N. Jiménez, J. M. Benlloch, and F. Camarena, Phys. Rev. Appl. 12, 014016 (2019).
- 30 M. D. Brown, J. Jaros, B. T. Cox, and B. E. Treeby, J. Acoust. Soc. Am. 139, 1637 (2016).
- ³¹R. E. Apfel and C. K. Holland, Ultrasound Med. Biol. 17, 179 (1991).
- 32B. D. Lindsey, J. D. Rojas, and P. A. Dayton, Ultrasound Med. Biol. 41, 1711 (2015)
- ³³J. Kim, S. Li, S. Kasoji, P. A. Dayton, and X. Jiang, Ultrasonics **63**, 7 (2015).
- 34P. Marmottant, S. van der Meer, M. Emmer, M. Versluis, N. de Jong, S. Hilgenfeldt, and D. Lohse, J. Acoust. Soc. Am. 118, 3499 (2005).
- ³⁵Z. Wang, A. C. Bovik, H. R. Sheikh, and E. P. Simoncelli, IEEE Trans. Image Process, 13, 600 (2004).
- ³⁶M. D. Brown, B. T. Cox, and B. E. Treeby, Appl. Phys. Lett. **116**, 261901 (2020).